the substrates were spin-coated at 2000 rpm for 30 s. The as-coated perovskite films were then annealed at 70 ^{o}C for 20 min.

3.2.2.4 Spiro-OMeTAD

3.2.2.4.1 Solution processing

The precursor solution was prepared by mixing 73 mg of spiro-OMeTAD into 1ml of chlorobenzene with additives consisting of 17.5 mL LiTFSI/acetonitrile (520 mg/mL) and 28.8 mL of 4-tert-butylpyridine.

3.2.2.4.2 Spin coating procedure and parameters

The HTM layer prepared spin-coating 60 μL of the spiro-OMeTAD solution onto the FTO/c-TiO_2/p-TiO_2/$MAPbI_3$ substrate at 2000 rpm for 45 s.

3.2.2.5 Evaporation of Silver electrode

The samples were allowed to dry in open air for a few minutes then put in a masked holder for the substrates to only get the evaporated metal on the wanted area that was at the center of the substrate as previously displayed in **Figure 3.3** and then placed in the evaporator (Leybold vacuum, Univex 350). The metal evaporated metal was Silver (Ag). The evaporation began by lowering the amount of pressure pressure inside the evaporator and when the pressure reached vacuum of $< 3.5\times10^{-6}$ mbar the current within the holder was manually increased. At ~165 A the evaporation of the silver started and the voltage was changed to get an evaporation speed of 0.02 nm. s^{-1} until a layer of thickness of 10 nm had been evaporated. The reason for the slow evaporation speed at the start was to avoid the Ag particles from penetrating the spiro-OMeTAD and be in direct contact with the perovskite layer. Then the evaporation speed was increased to 0.2 nm. s^{-1} by changing the current. One pellet of Ag resulted in a layer approximately 70 nm thick.

3.3 Characterization of interfaces and devices

3.3.1 Film characterization techniques

3.3.1.1 Surface profilorimery

Veeco Dektak profilometers was used for the measurement of layer thicknesses. Samples were scratched with a scalpel and then cleaned with compressed nitrogen in order to remove any remaining debris. The stylus of the Dektak was then passed above the sample, going across the scratch in the film, permitting a thickness measurement to be taken as shown in **Figure 3.** 4 **(a)**. At least 4 readings from different scratches were taken for each sample individually and the average of those thicknesses was used. In the case of uneven films the height was averaged over a range of positions in order to guarantee a more accurate reading (see **Figure 3.** 4 **(b)**).

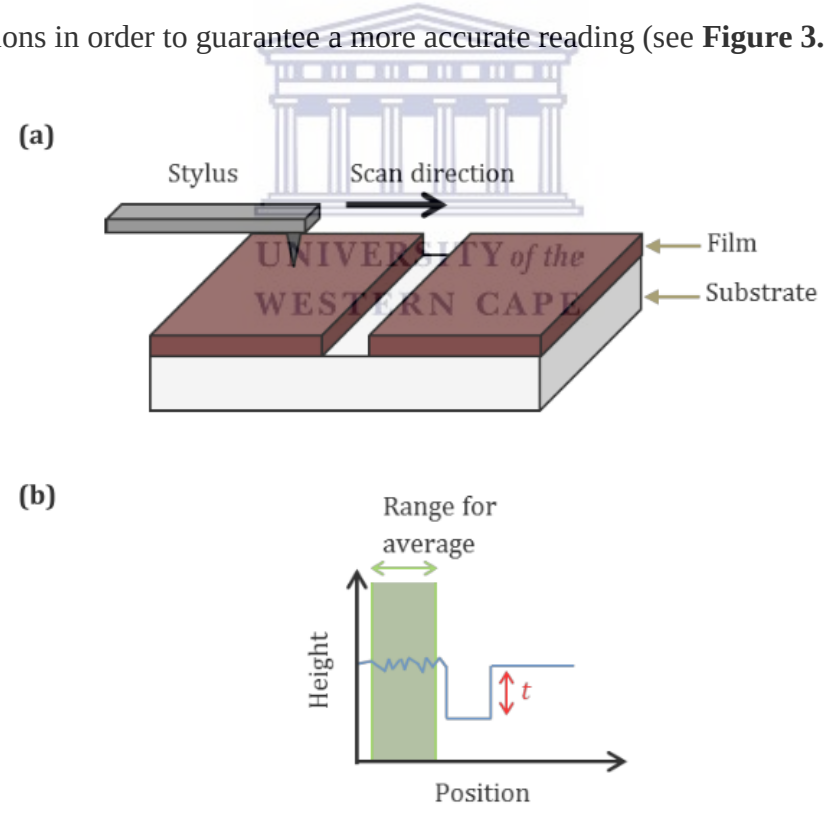

Figure 3. 4: A schematic of the profilometry equipment (a) and an example scan showing the use of a range in order to ensure a more accurate height reading when measuring rough films (b).

3.3.1.2 Microscopic characterization

Microscopy is a specialized field of characterization techniques that uses microscopes to inspect objects and the surface of objects that would normally be difficult to see with the naked eye (objects that are not within the resolution range of the normal eye) [1]. There are three types of microscopy: optical, electron, and scanning probe microscopy. **Figure 3.5** shows cross sectional diagram of imaging modes for the three types of microscopes regularly employed for materials characterization: the light microscope (left), the transmission electron microscope (TEM, center), and the scanning electron microscope (SEM, right).

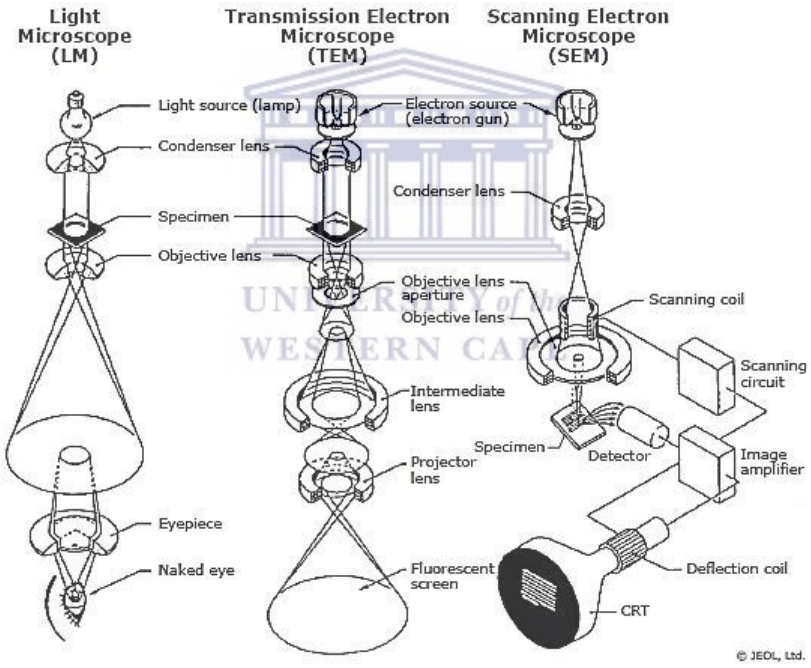

Figure 3.5: Schematic cross-sections of imaging modes in the light microscope, the TEM, and the SEM [2].

Frequent elements include a source of illumination (visible light source or an electron gun) and a condenser lens over the specimen to center the light or electron beam. After the condenser lens, the structure of the SEM diverges from that of the light microscope and the TEM. In the latter two, the objective lens that produce the image is positioned below the specimen, and a static,

near-parallel beam of illumination is projected onto a viewing point or onto a camera for recording. Though the TEM includes some additional lenses, the overall method by which the image is obtained and projected for viewing and recording is the same as that of the light microscope.

The SEM is significantly different in that the objective lens sits over the specimen or sample, and the beam is created into a fine, centered probe that is passed across the specimen using scanning coils, producing an image point by point. The image can be recorded on various detectors placed above the specimen.

These types of microscopes give complementary information over diverse size ranges. The unaided human eye resolution features down to about 100 μm in size, and the best performing light microscopes allow us to see features as small as 1 μm. Because SEMs and TEMs utilize electrons, which have higher energies and shorter wavelengths than visible light, much smaller objects can be seen as well from its use. The highest-resolution SEMs can allow users to see objects with only a few nanometers in size, while aberration-corrected TEMs allow for imaging and analysis of objects and substance at the atomic level. All three types of microscope can be used complementarily to provide fundamental information about size, morphology, and texture of materials or objects. Although the SEM and TEM are usually classified as electron optical instruments, the TEM and the light microscope share a similar mechanism for image formation.

3.3.1.2.1 Scanning Electron Microscopy (SEM)

Scanning electron microscopy (SEM) is a characterization technique that utilizes electrons to investigate a sample's surface in order to imaging easier at higher resolution than is possible with the normal optical microscope. Given that the resolution is only limited to around half the wavelength of the probe, it is possible to obtain much higher resolution with electron microscopy

than optical microscopy. Additionally, SEMs offer the ability to obtain better '3D' image than optical microscopes due to the larger depth of focus resulting from the lower aperture angle.

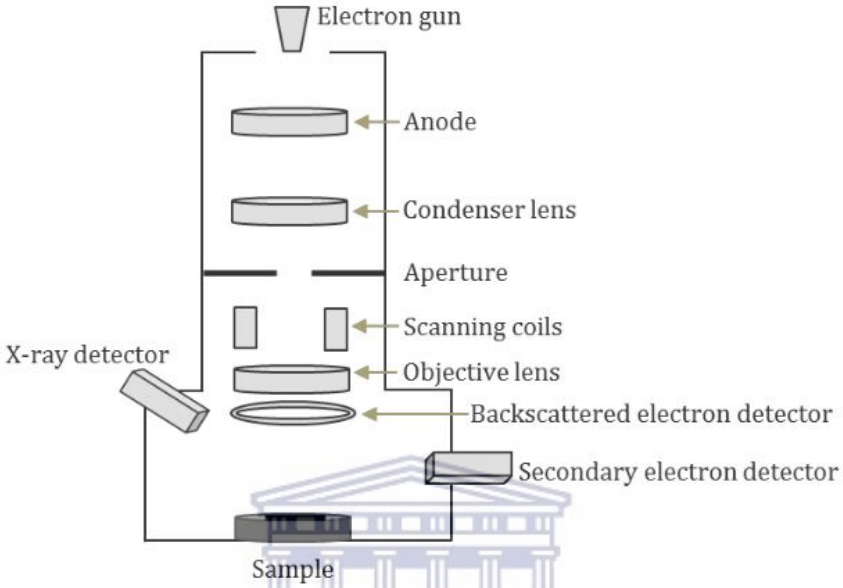

Figure 3.6: A basic schematic of a scanning electron microscope.

In **Figure 3.6** is shown a simplified image/schematic diagram of the SEM instrument. In order to avoid interactions between the electron beam and the air, the electron gun, optics and sample chamber are held under vacuum, which reduces the image quality and could cause the sample to be damaged. The electron beam in a SEM is generated by either a thermionic emission gun (heating a filament to release electrons) or field emission gun (using a strong electric field to extract electrons from a tungsten crystal). A field emission gun SEM (FEGSEM or FESEM) offers better resolution than its thermionic counterpart due to the production of narrower beams of electrons with smaller spread in energy. In this work the field emission gun SEMs has been used. Electrons are emmited and allowed to travel in a helical path down the microscope column under the influence of magnetic fields from the electromagnetic lenses. To control the spot size

of the beam on the sample, the condenser lens(es) and aperture(s) act in tandem. A decreased spot size increases the resolution but reduce the clarity of the image and results in ‘graininess’ as less electrons invade on the sample. Scanning coils are used to deploy the electron beam across the sample in order to produce an image, whilst electron beam is focused onto the sample by the objective lens. Increasing the accelerating voltage reduces the diameter of electron probe, therefore the improving resolution of the output images obtained from the sample analysis. This also, however, reduces the clarity of surface structures, because the penetration of the beam into the sample is augmented. In addition the charging is increased together with any sample damage which may occur. When the electron beam strikes the sample it causes both electrons and X-rays to be ejected from the material. The ejected electrons are usually distributed into two types – secondary and backscattered, with imaging most of the time achieved using the secondary electrons (SEs). These have a shallow generation region (~10 nm) since those generated deeper in the sample will be unable to escape due to their fairly low energy (~50 eV or less). Secondary electron detectors have a scintillator (fluorescent material) over which a voltage is applied. In front of the detector is also a collector, through which a high voltage is applied to attract the secondary electrons discharged from the sample. These impact on the scintillator and generate light which is allowed to pass through a photomultiplier before being transformed into an electrical signal. When the electron beam attains the sample at an angle, more secondary electrons are generated than when it is normal to the surface, implying that SE images appear particularly topographical. Backscattered electrons have a higher energy than secondary electrons, having a range of energies up to that of the incident beam. The increased energy of the backscattered electrons implies that they are less impacted by charging and specimen contamination than SEs, and that their generation region is considerably larger. While this

decreases resolution, it does allow for detection of electrons from deeper into the sample. Backscattered electron intensity is dependent on atomic number, and thus backscattered images can provide a composition contrast as well as a topographic one.

It is important to note that the sample under examination is conductive enough, or coated and stuck to the sample stub with a conductive material to avoid charging. This happens when electrons from the probe beam build up on the specimen, interfering with secondary electron emission and thus adversely affecting the image quality and resolution.

For the purpose of this research project the instrument used for this specific analysis was the ZEISS ULTRA scanning electron microscope with acceleration voltage of 5.0 kV.

3.3.1.2.2 Transmission electron microscope

Transmission electron microscopy (TEM) is a microscopy technique in which a beam of electrons is transmitted across an ultrathin sample or specimen, interacting with the sample as it passes through. An image is produced from the interaction of the electrons transmitted through the sample; the image is enlarged and focused onto an imaging device, such as a fluorescent screen, on a layer of photographic film, or to be detected by a sensor such as a CCD camera.

TEM in essence is used to reveal sub-micrometer, internal fine structure in solids. The amount of information which can be extracted by TEM depends critically on four very important parameters; the resolving power of the microscope (usually smaller than 0.3 nm); the energy spread of the electron beam (often several eV); the thickness of the specimen (almost always significantly less than 1μm), and; the composition and stability of the specimen [3].

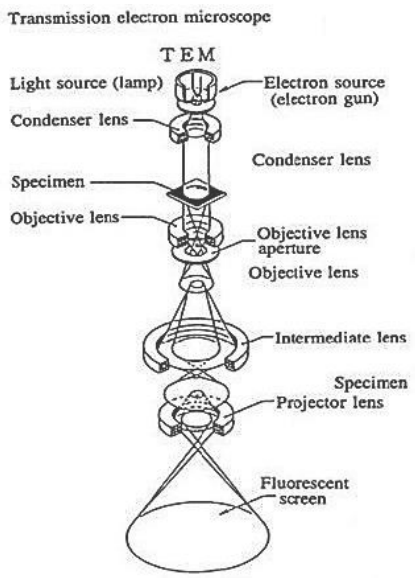

Figure 3.7: General layout of a TEM describing the path of electron beam in a TEM. (Image taken from JEOL 2000FX Handbook).

In order to obtain the TEM images needed for a sample, the beam of electrons from the electron gun is focused into a small, thin, clear beam by the use of the condenser lens as shown in **Figure 3.7**. The beam is limited by the condenser aperture, which eliminates high angle electrons. The beam then collides with the sample and parts of it are diffused depending upon the thickness and electron translucence of the specimen. This transmitted portion is focused by the objective lens into an image on phosphor screen or charge coupled device (CCD) camera. Optional objective apertures can be utilized to increase the contrast by blocking out high-angle diffracted electrons. The image is then passed down the column across the intermediate and projector lenses, is broadened all the way. The image strikes the phosphor screen and light is produced, allowing the user to see the image. The darker areas of the image characterize those areas of the sample that fewer electrons are transmitted across while the brighter areas of the image characterize those areas of the sample that more electrons were transmitted across.

For the purpose of this research project the TEM instrument used for this analysis is the TECNAI G2 F2O X-TWIN MAT 200 kV field emission, where nickel grid was used to coat the material for better conductivity.

3.3.1.3 Spectroscopic characterization

Spectroscopy is the study of the properties of matter and its interaction with different frequency components of the electromagnetic spectrum [4]. Spectroscopy is a common technique that can be used in many ways to obtain information needed about a substance such as electronic energies, vibrational energies, rotational states, structure and symmetry of molecules, and finally dynamic information.

3.3.1.3.1 Energy-Dispersive X-ray spectroscopy (EDS or EDX)

Energy dispersive X-ray spectroscopy (EDS) is a typical technique for element detection in material analysis. EDS systems are mounted on scanning electron microscopes (SEM) and use the primary beam of the microscope to produce characteristic X-rays. The composition of the sample is found by analyzing the energy of the characteristic X-rays that are emitted from the sample after the incoming radiation [5]. The spatial (lateral + vertical) resolution of EDS depends on the sample material and the energy of the primary beam of the SEM as shown in **Figure 3.8**.

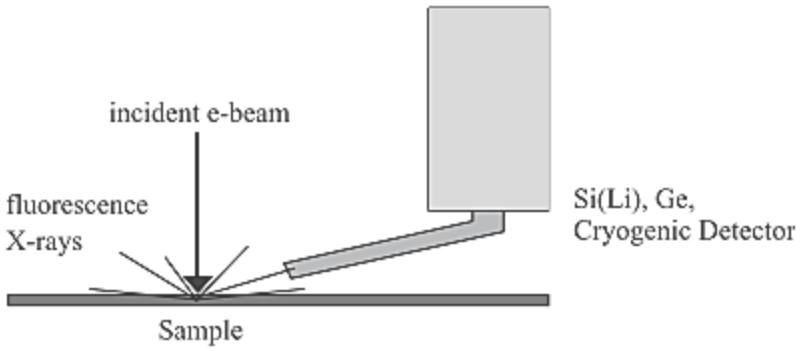

Figure 3.8: Working principle of EDS.

The instrument used is the EDS analyzer coupled into the High-Resolution Scanning Electron Microscope used for SEM analysis.

3.3.1.3.2 Ultraviolet-Visible spectroscopy (UV-Vis)

UV/Vis spectroscopy is a measurement technique in which the recording of the absorption spectra of different samples using ultraviolet (UV) and visible (Vis) light is achieved by a spectrophotometer, i.e. an instrument able to measure the spectrum of a sample in the UV/Vis range [6]. A UV/Vis spectrophotometer determines the intensity of light passing through a sample solution in a cuvette, and evaluates it against the intensity of the light before it passes through the sample. The light should also be passed though the cuvette or sample holder in order to account for any absorption by them. The major components of a UV/Vis spectrophotometer are a light source, a sample holder, a dispersive device to separate the different wavelengths of the light (e.g. a monochromator), and a suitable detector as shown in **Figure 3.9**.

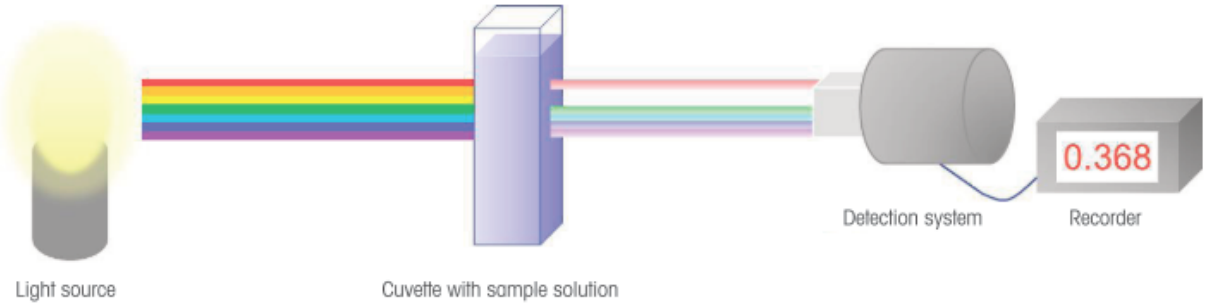

Figure 3.9: Measurement principle in UV/VIS spectroscopy [6].

The UV–Vis absorption spectra were obtained by using UV-Vis Double beam Spectrophotometer from ThermoFisher Scientific.

3.3.1.4 Electrochemical characterization

Electrochemistry is a vast and interdisciplinary field of research and development activity, that deals the interrelation of electrical and chemical effects [7]. A significant aspect of this field is the study of chemical changes caused by the movement of an electric current and the generation of electrical energy by chemical reactions, which include an array of diverse phenomena (e.g., electrophoresis and corrosion), devices (electrochromic displays, electroanalytical sensors, etc.), and technologies (the electroplating of metals and the large-scale production of aluminum and chlorine) [8].

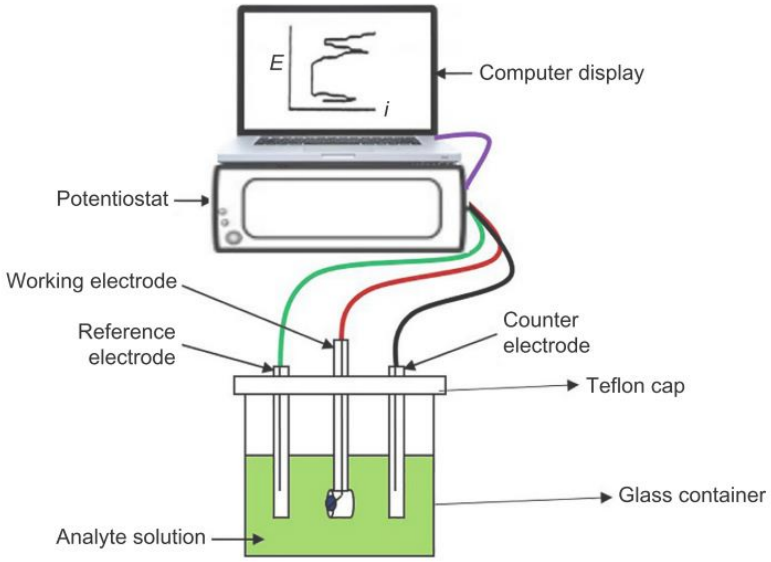

Figure 3.10:Illustration depicting the simplicity of a three-electrode electrochemical cell system that would form part of an electrochemical workstation.

Although largely based on conventional electrochemical characterization methods developed for bulk materials, including potentiometric, polarography, voltammetry, cyclic voltammetry (CV), chrono-potentiometry, chrono-amperometry, linear sweep, and pulsed methods, the "nanoscale" concept has initiated a new scenario in which physicochemical principles, laws, and properties which can be quite different from those of the macro and micro worlds. Electrochemical characterization of nanomaterials necessitates not only sensitivity and selectivity but also accuracy.

Deciding on the best technique for a particular situation needs knowledge of the analyzed particles or materials, the ultimate application of the particles, and the restrictions of the considered techniques. Therefore, a rational choice of technique(s) and methodology(ies) is essential.

The basis of electrochemical investigation is electrode surface reaction. Because the working electrode (WE) substrates can strongly influence the efficiency of the reactions, the properties of electrode substrates and ionic substance at the electrode surface are of great significance for successful electrochemical characterization. Different researchers, including David Harvey et al. in 2012, have shown that there are six basic and interrelated concepts of note in the study of electrochemistry: (1) the electrode's potential determines the analyte's form at the electrode's surface; (2) the electrochemical cell design; (3) the concentration of analyte at the electrode's surface may not be the same as its concentration in bulk solution; (4) the analyte may not be restricted from participating in other reactions; (5) the current as a measure of the rate of the analyte's oxidation or reduction; and (6) current and potential cannot be controlled simultaneously.

3.3.1.4 Electrochemical Characterization

3.3.1.4.1 Cyclic Voltammetry

CV is a technique used to study the electrochemical properties associated with surfaces that are electroactive. CV is a very multipurpose electrochemical method that enables understanding of the mechanisms of redox reactions, reversibility of a reaction, and electron transfer kinetics of an electroactive species in solution [9,10]. CV offers rapid information on thermodynamic redox processes, on the kinetics of heterogeneous electron-transfer reactions, and on coupled chemical reactions or adsorption processes [9]. It is the foremost electrochemical experiment performed to characterize electrode material for every type of application [9].

3.3.2 Device characterization

3.3.2.1 Solar Cells Current-Voltage measurements

The main characteristic of a solar cell is its aptitude to convert light into electricity. This is known as the power conversion efficiency (PCE) and is the ratio of incident light power to output electrical power. To determine the PCE, and other helpful metrics, current density-voltage (I-V) measurements are performed. A series of voltages are applied to the solar cell while it is under illumination. The output current is quantified at each voltage step, resulting in the characteristic 'I-V curve' seen in many research papers. An example of this can be seen below in **Figure 3.11**, along with some significant properties that can be determined from the I-V measurement. It should be noted that generally, current density (J) is used instead of current when characterizing solar cells, as the area of the cell will have an effect on the magnitude of the output current (the larger the cell, the more current).

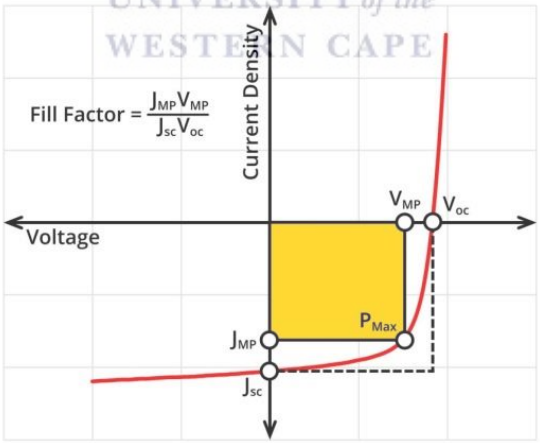

Figure 3.11: Typical I-V curve of a solar cell plotted using current density, highlighting the short-circuit current density (J_{sc}), open-circuit voltage (V_{oc}), current and voltage at maximum power (J_{MP} and V_{MP} respectively), maximum power point (P_{Max}), and fill factor.

3.3.3. Other characterization

3.3.3.1 X-ray diffractometry (XRD)

X-ray diffraction (XRD) is one of the most important non-destructive tools to analyze diverse classes of matter, ranging from fluids, to powders and crystals. From research to production and engineering, XRD is a crucial method for structural materials characterization and quality control which makes use of the Debye-Scherrer method. This technique uses X-ray (or neutron) diffraction on powder or microcrystalline samples, where preferably every possible crystalline orientation is characterized equally. In the so called diffractogram the diffracted intensity is shown as function either of the scattering angle 2θ or as a function of the scattering vector q which makes it autonomous from the used X-ray wavelength. The diffractogram is like a distinctive "fingerprint" of materials.

X-ray diffractometry is a characterization technique that bases its working principle solely onit ability to diffracts X-rays from crystals in a characteristic manner allowing a precise study of the structure of crystalline phases. The recorded diffraction patterns contain additive contributions of several micro- and macro-structural characteristics of a sample. With the peak position, lattice parameters, space group, chemical composition, macro-stresses, or qualitative phase analysis can be examined. Based on the peak intensity, knowledge about crystal structure (atomic positions, temperature factor, or occupancy) as well as texture and quantitative phase analyses can be obtained. Finally, the peak shape gives information about sample broadening contributions (micro-strains and crystallite size) [11].

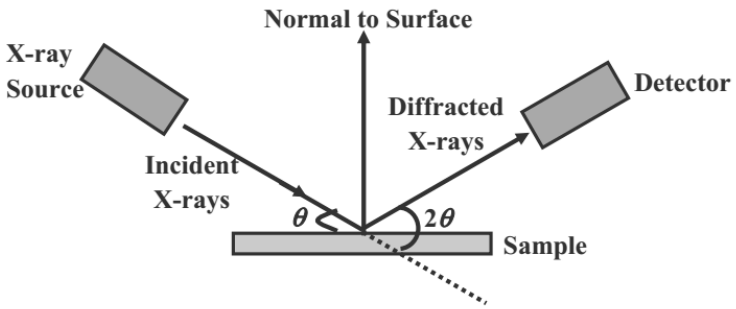

Figure 3.12: Schematic representation of the working principle of X-ray diffraction [11].

The SAED micrograph as seen from the example in **Figure 4.4** is the diffraction pattern obtained in the reverse space of the lattice planes. It is used in order to find the d-spacing of the crystal planes. The SAED pattern can be used to see if the sample is amorphous, i.e. diffuse rings, crystalline (bright spots), polycrystalline (small spots making up rings, each spot arising from Bragg reflection from an individual crystallite. The results obtained from XRD can be used in conjunction with the SAED micrograph to corroborate specific information obtained from the sample.

The XRD data were collected with the help of the BRUKER AXS DS Advance diffractometer with 2θ values ranging from 20-90 º, with a step size of 0.028 º operating at 45 kV and 40mA form the Ithemba Labs.

3.3.3.2 Fourier Transform Infrared Spectroscopy (FTIR)

FTIR analysis measures the intensity of absorption at a range of wavelengths in the infrared region that are captured by a material as seen. The application of infrared radiation (IR) to samples of a material allows for this to be accomplished. The sample's absorbance of the infrared light's energy at diverse wavelengths is measured to determine the material's molecular composition and structure [12].

This technique also allow for the identification of unknown materials by comparing the spectrum against a spectra in the reference database. Materials can be quantified using the FTIR materials characterization technique as long as a standard curve of known concentrations of the component of interest can be created.

FTIR analysis can be used to identify new materials, additives within polymers, surface contamination on a material, and more. The results of the tests can identify a sample's molecular composition and structure.

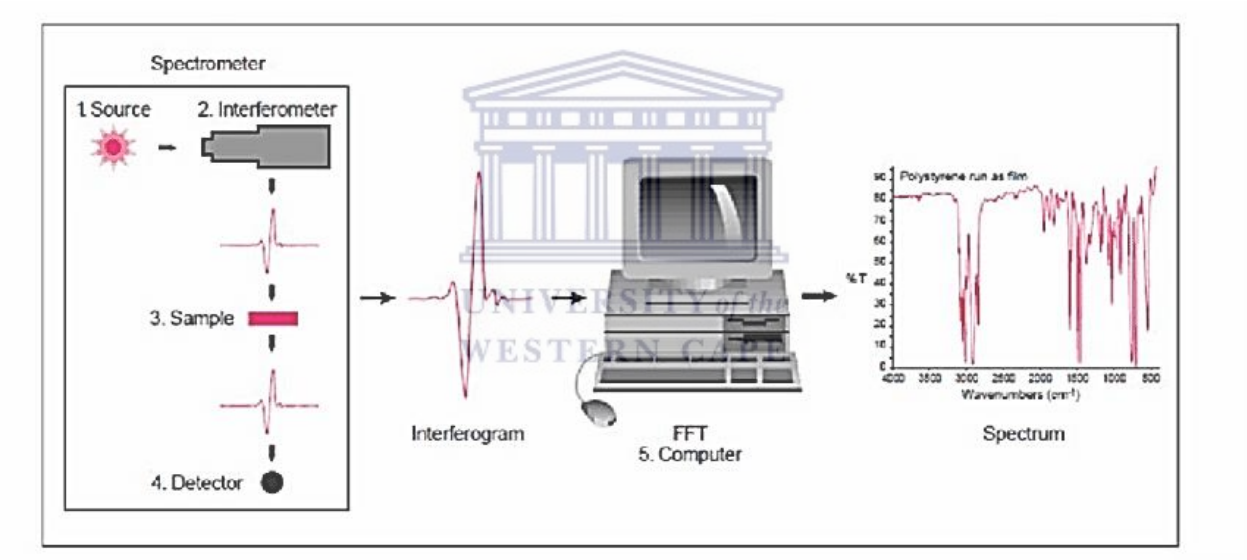

Figure 3.13: Working principle of the Fourier transform infra-red spectrometer Infra-red (IR) spectrometer [14].

The instrument used for the analysis was Perkin Elmer spectrum Two FTIR spectrometer. FTIR Spectra were recorded in the range of 4000-400 cm^{-1} using the substrates coated with the different layers of materials being studied.

3.4 References

[1] The University of Edinburgh, What is Microscopy? | The University of Edinburgh, Online. (n.d.). https://www.ed.ac.uk/clinical-sciences/edinburgh-imaging/for-patients-study-participants/tell-me-more-about-my-scan/what-is-microscopy (accessed November 28, 2019).

[2] E.F. Schumacher, Microscopy for materials characterization: Illuminating structures with light and electrons, Am. Lab. 46 (2014). https://www.americanlaboratory.com/914-Application-Notes/167499-Microscopy-for-Materials-Characterization-Illuminating-Structures-With-Light-and-Electrons/ (accessed November 28, 2019).

[3] P.J. Goodhew, General Introduction to Transmission Electron Microscopy (TEM), in: Aberration-Corrected Anal. Transm. Electron Microsc., 2018: pp. 1–18. doi:10.1002/9781119978848.ch1.

[4] J. Chen, B. Gu, E.J. Leboeuf, H. Pan, S. Dai, Spectroscopic characterization of the structural and functional properties of natural organic matter fractions, Chemosphere. 48 (2002) 59–68.

[5] C. Hollerith, D. Wernicke, M. Buhler, F. v. Feilitzsch, M. Huber, J. H.ohne, T. Hertrich, J. Jochum, K. Phelan, M. Stark, B. Simmnacher, W. Weiland, W. Westphal, Energy dispersive X-ray spectroscopy with microcalorimeters, Nucl. Instruments Methods Phys. Res. 520 (2004) 606–609. doi:10.1016/j.nima.2003.11.327.

[6] C.A. De Caro, UV / VIS Spectrophotometry Fundamentals and Aplications, 2015.

[7] P.S. Nnamchi, C.S. Obayi, Electrochemical Characterization of Nanomaterials, in: Charact. Nanomater., Elsevier Ltd., 2018: pp. 103–127. doi:10.1016/b978-0-08-101973-

3.00004-3.

[8] A. Larry, J. Bard, Faulkner, L. R., Electrochemical Methods: Fundamentals and Applications, second edi, JOHN WILEY & SONS, INC, 2001. doi:10.1108/acmm.2003.12850eae.001.

[9] F. Manea, Electrochemical Techniques for Characterization and Detection Application of Nanostructured Carbon Composite, in: Mod. Electrochem. Methods Nano, Surf. Corros. Sci., InTech, 2014. doi:10.5772/58633.

[10] D.K. Gosser, Cyclic Voltammetry; Simulation and Analysis of Reaction Mechanisms, Synth. React. Inorg. Met. Chem. 24 (1994) 1237–1238. doi:10.1080/00945719408001398.

[11] Y. Li, S.M. Chen, M.A. Ali, F.M.A. AlHemaid, Biosynthesis and electrochemical characterization of silver nanoparticles from leaf extract of adenium obesum and its application to antibacterial effect, Int. J. Electrochem. Sci. 8 (2013) 2691–2701.

[12] R.E. Dinnebier, S.J.L. Billinge, Powder Diffraction : Theory and Practice, Royal Society of Chemistry, 2008. doi:10.1039/9781847558237.

[13] J. Mathias, How Does FTIR Work? | Innovatech Labs, (2015). https://www.innovatechlabs.com/newsroom/672/stuff-works-ftir-analysis/ (accessed November 29, 2019).

[14] G. Ramaiah, D. Bhatia, Structural Analysis Of Merino Wool, Pashmina And Angora Fibers Using Analytical Instruments Like Scanning Electron Microscope And Infra-Red Spectroscopy, Int. J. Eng. Technol. Sci. Res. 2394-3386. 4 (2017) 112–125. https://www.researchgate.net/publication/319135784_Structural_Analysis_Of_Merino_W

ool_Pashmina_And_Angora_Fibers_Using_Analytical_Instruments_Like_Scanning_Electron_Microscope_And_Infra-Red_Spectroscopy (accessed March 1, 2020).

Chapter 4 Results and Discussions

This chapter introduces the results gotten from the different characterization techniques performed, their analysis and discussion. The techniques used comprised HR-SEM, HR-TEM, XRD, EDS, FTIR, UV-Vis, CV and I-V curve measurements. The most important deductions and conclusionsare based on calculated photovoltaic parameters. The majority of the samples were fabricated in air with relative humidity of about 60 %. Because of the moisture in air and other atmospheric effects, the perovskite fabrication is not totally reproducible and the degree of degradation varies. Thus, the photovoltaic parameters of the prepared solar cell series are not fully comparable to each other.

4.1 Interface characterization

4.1.1 Surface morphology

High Resolution Scanning Electron Microscope (HR-SEM)

The morphology of the surface of the prepared pristine TiO_2 and Ag-TiO_2 thin films were studied using a scanning electron microscope.

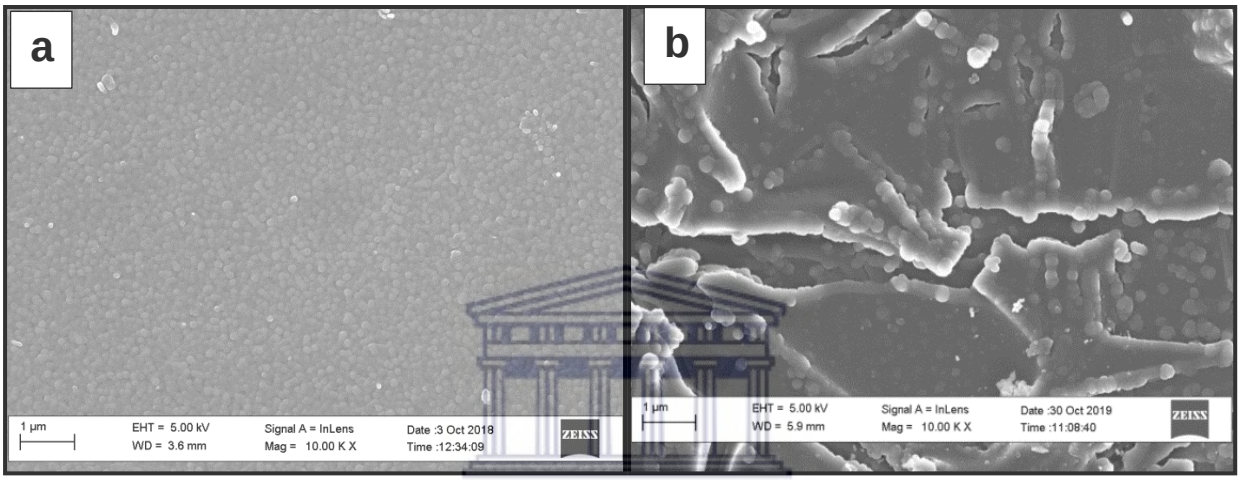

Figure 4.1: SEM images of a) Pristine compact-TiO_2 and b) 2.5 % Ag-TiO_2 composite films.

Figure 4.1 a) and b) shows the SEM images of the undoped (compact pristine TiO_2 layer) and Ag doped TiO_2 films formed on the ITO substrates via the spin-coating method. The images of the pure TiO_2 film in **Figure 4.1** shows the surface morphologies of compact TiO_2 layers which was fabricated on ITO substrates using spin-coating methods. As can be seen in **Figure 4.1 a)** the TiO_2 is extremely smooth and dense with very good surface coverage, showing no observable defects. The surface doesn't show any discontinuities, cracks, pinholes, and pores. As is well-known, ITO substrates are based on In-doped SnO_2 grains with sizes fluctuating between tens to hundreds of nanometers, and due to the grain boundaries, the substrate surface is uneven. The spin- coating-based compact TiO_2 layer did not alter the surface topography of the ITO grains as the layer was very thin (45-60 nm thick across the surface of the substrate). Relatively

large TiO_2 particles (>10 nm) fill up the gaps between the ITO grains and makes the surface much smoother on the micron scale. This means that, the TiO_2 layer's thickness the is not perfectly uniform across the surface of the substrate, and this theoretically should be problematic in when it comes to the charge collection through the blocking layer. These affirmations will further be confirmed by the cyclic voltammetry study which was done to both test for defects in the TiO_2 compact blocking layer and test for the ability of the material to reduce recombination.

The microstructure of the Ag-TiO_2 films was made up of several mud-crack shaped layers. These defects could be due to the heat treatment regime to which the Ag-TiO_2 films were exposed. Thermal shock may be the principal reason for the mud cracks on the surface of the films. These cracks on the layer surface are very noticeable when the Ag concentration was augmented as was the case in **Figure 4.1 b)** above; the larger Ag particles were observed on the mud-crack-shaped layers. Even with these apparent defects at the surface of the layer the Ag nanoparticles helped in increasing the conductivity of the TiO_2 layer as will once again be observed in the results of the cyclic voltammetry study explained later in this chapter.

4.1.2 Internal structure

1.1.1.1 High Resolution Transmission Electron Microscope (HR-TEM)

The internal structure of the synthesized nanoparticles was evaluated using transmission electron microscope (TEM).

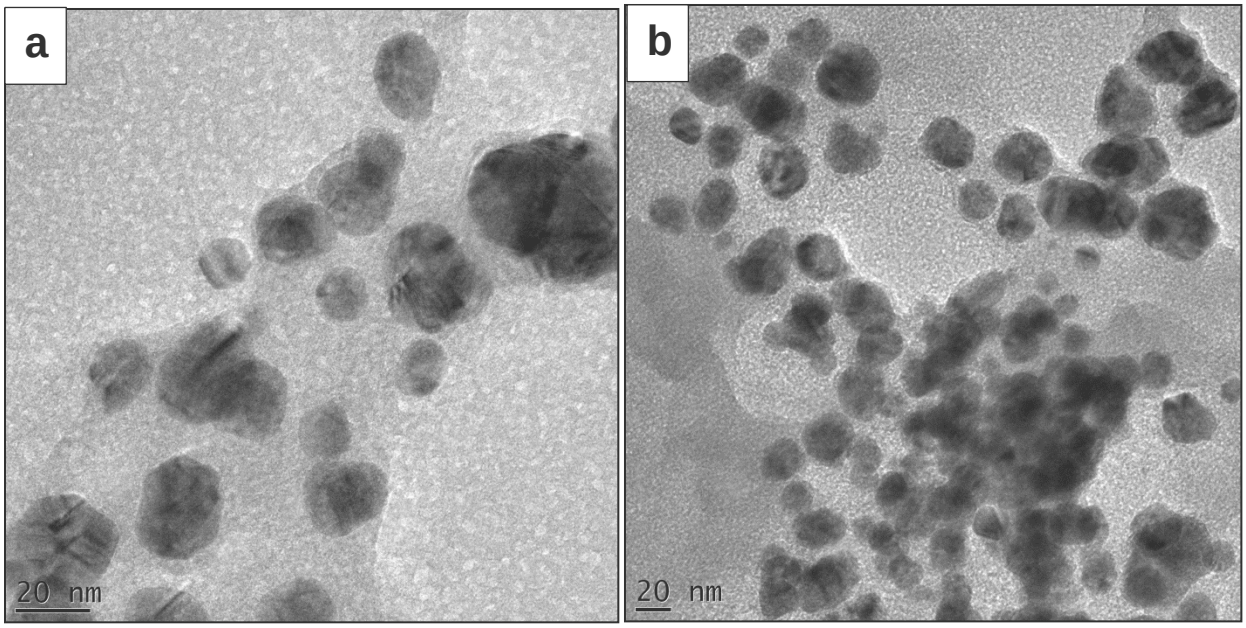

Figure 4.2:TEM micrograph of a) Pristine compact-TiO_2 and b) 2.5 % Ag-TiO_2 solutions.

The TEM images of the pristine compact-TiO_2 and 2.5 % Ag-doped TiO_2 particles are shown in **Figure 4.2 a)** and **b)** respectively. The micrograph obtained for the nanoparticles shows the poly-disperse nature of the nanoparticles in both cases. The micrograph shows some sphere-like structure for both the pristine TiO_2 and Ag-TiO_2 as can be seen in **Figure 4.2 a)** and **b)** above. The internal structure of the synthesized nanoparticles also revealed some agglomerations as well as the presence of nanoparticles of smaller sizes. Although the observed TiO_2 nanoparticles have a spherical shape with a diameter of about 25 nm, most of the TiO_2 nanoparticles appeared to be agglomerated and formed large particle with a diameter as large as 50 nm, which might be due to their large surface area and high interface energy. Compared with TiO_2 nanoparticles, Ag-TiO_2 nanoparticles showed much more agglomeration with a diameter around 30 nm for the smaller nanoparticles and up to about 90 nanometers for the larger nanoparticles as depicted in **Figure 4.2 b)**. Although, the micrograph obtained did show sporadic agglomeration of nanoparticles in some areas for both the pristine and Ag-doped nanoparticles, distinct information about the

internal structure could still be extracted to determine the particle size of the nanoparticles and lattice fringes spacing as will be seen later.

4.1.3 Phase composition

1.1.1.2 X-Ray Diffraction (XRD)

The phase composition and crystalline structure of the synthesized nanoparticles were investigated through powder X-ray diffraction (XRD). The XRD results obtained were refined with crystal-impact software called MATCH to remove the noise and obtain only the available peaks from the diffraction pattern of the sample analyzed.

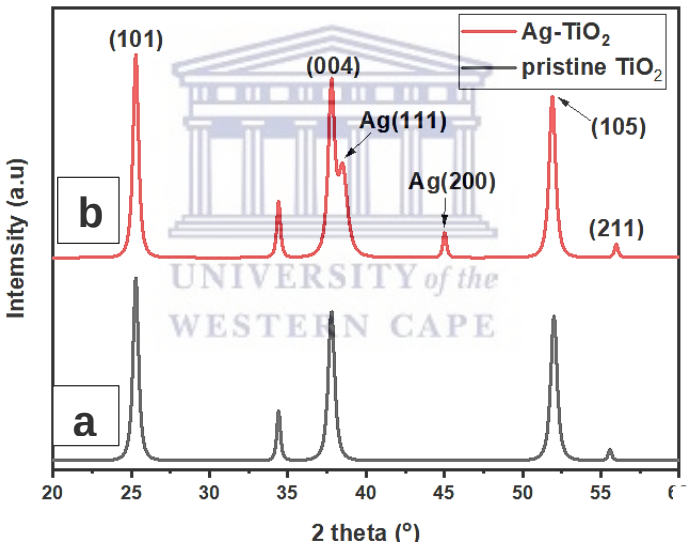

Figure 4.3: XRD patterns of the a) pristine TiO_2 and b) 2.5 % Ag-TiO_2 composites films with substracted ITO substrates peaks.

The XRD patterns of the pristine TiO_2 and the Ag/nano-TiO_2 composite compact film are presented in **Figure 4.3 a) and b)**. The spiky and intense peaks in spectra are an sign of the presence of crystalline films. Most of the main diffraction peaks at 25.29 ^{o} (101), 37.69 ^{o} (004), 51.97 ^{o} (105) and 54.91 ^{o} (211) agree with the JCPDS values (PDF Card No: 00-021-1272) which match to the crystal structure of anatase phase of TiO_2 [1]. As opposed to the diffraction

peaks of the pristine TiO_2, the peaks of the Ag-TiO_2 composite compact film in ($2\theta = 38^o$) and ($2\theta = 45^o$) are considerably larger, while the other peaks stay almost the same as in the pristine which was expected as seen in **Figure 4.3 b)**. One very important aspect to note is the fact that the peaks of the Ag-TiO_2 composite compact film in ($2\theta = 38^o$) and ($2\theta = 45^o$) are not observed at all in the pristine compact-TiO_2 films. The peaks at diffraction angles ($2\theta = 38^o$) and ($2\theta = 45^o$) are attributed to the specific diffraction peaks of the (111) and (200) crystal planes of Ag with the standard anatase PDF card, respectively. Additionally, there is no clear shift in any of the diffraction peaks, suggesting that no trace of the Ag oxide phase was found in the prepared samples. It is possible to observe that all the distinctive diffraction peaks of the anatase TiO_2 phase (101), (004), and (105) are seen in **Figure 4.3 a)** and **b).** The full-width at half-maximum is similar for the most intense peak of the anatase diffraction phase (101)of both the pristine TiO_2 compact film and the Ag-TiO_2 composite compact film. This is an indication that the crystal structure of TiO_2 barely changes with the development of the Ag-TiO_2 composites.

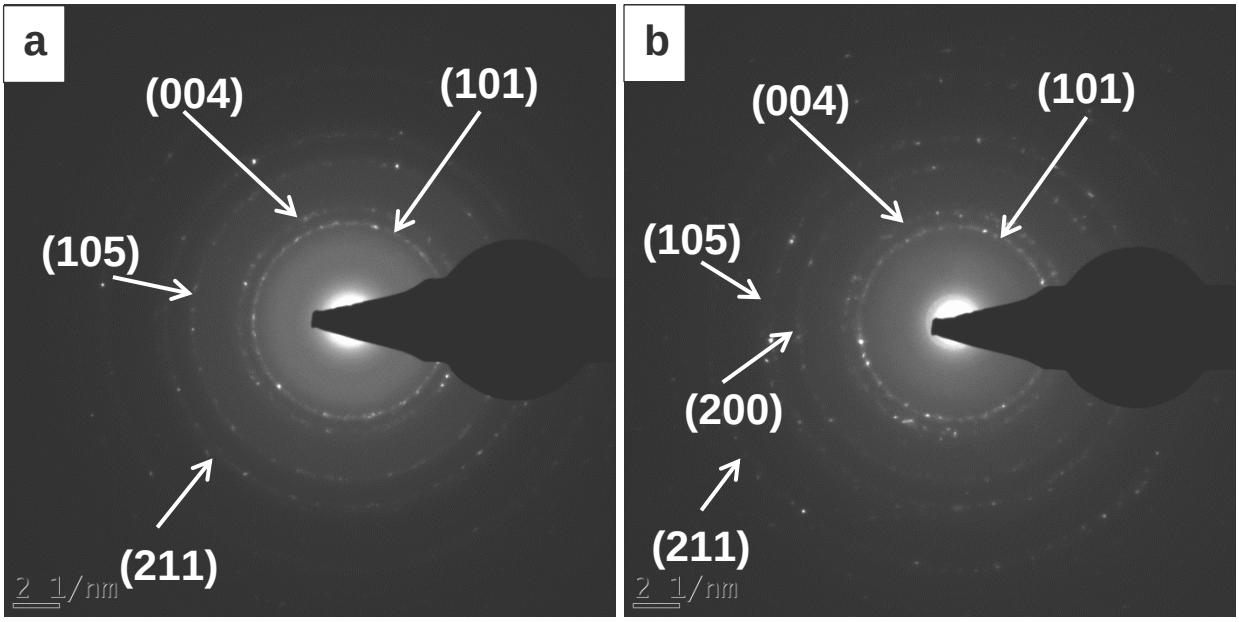

Figure 4.4: SAED micrograph of the a) pristine TiO_2, and b) Ag-TiO_2 nanoparticles confirming the hkl miller index (planes) found in the XRD spectra.

Selected Area Electron Diffraction (SAED) was obtained from HR-TEM which revealed and confirmed that the nanoparticles were crystalline as seen in **Figure 4.4 a)** and **b)**. The planes found in XRD plot in **Figure 4.3** above were also observed in the SAED image obtained, which confirms the anatase phase composition of the synthesized nanoparticles. The images obtained from SAED analysis, shows that both the pristine TiO_2 and Ag-TiO_2 were crystalline. The higher crystallinity displayed by Ag-TiO_2 translated into a high electro-activity which was the expected outcome with improved photocatalytic property as seen from the discussions of electrochemistry of the thin films and their optical properties which leads to a possible correlation between high crystallinity and electro-activity as the least crystalline of the nanoparticles TiO_2 displayed a lower electro-activity when compared to Ag-TiO_2 which was more crystalline.

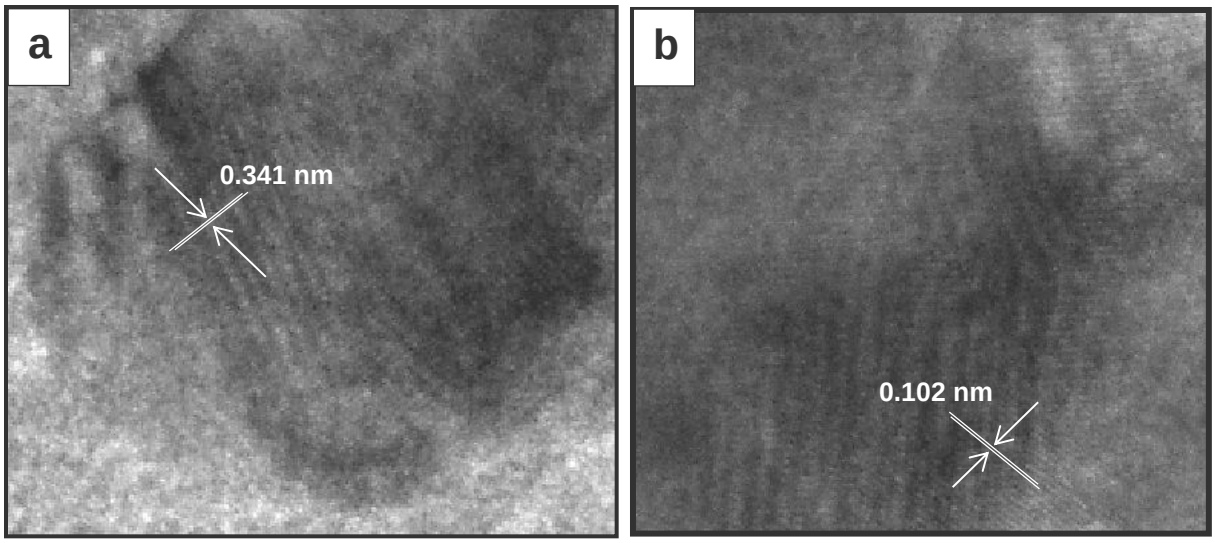

Figure 4.5: HR-TEM image of a) pristine compact-TiO_2, b) Ag-TiO_2 showing the lattice fringe and d-spacing values of the lattice.

The lattice fringe images obtained for the synthesized nanoparticles further confirms that the nanoparticles were crystalline and the d-spacing value of the lattice fringes were assigned as can be seen in **Figure 4.5 a)** and **b)** above.

4.1.4 Elemental composition

1.1.1.3 Energy Dispersive Spectroscopy (EDS)

The elemental composition of the prepared thin films was evaluated using Energy Dispersive X-ray spectroscopy (EDS) as shown in figure 4.11.

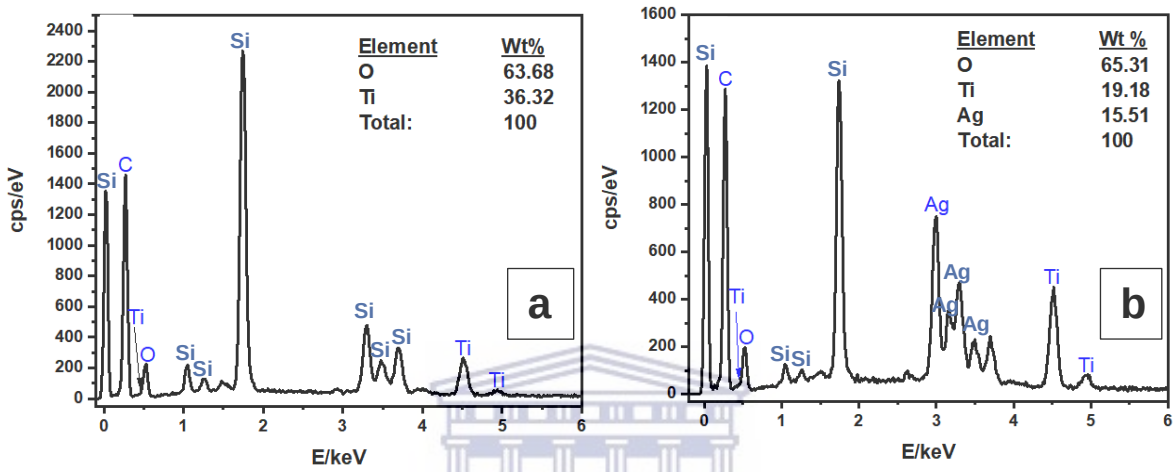

Figure 4.6: EDS images of a) Pristine TiO_2 and b) Ag-TiO_2 composite films with substracted ITO substrates peaks.

Figure 4.6 a) and b) displays the EDS results obtained for both the pristine TiO_2 and Ag-TiO_2 films surface with subtracted ITO substrate peaks. The EDS spectra of the prepared thin films showed all the elements expected for the samples analyzed. **Figure 4.5 a)** shows the pristine TiO_2 spectra, where the presence of titanium, oxygen and carbon can be observed. The same can be seen in **Figure 4.5 b)** which shows the Ag-doped TiO_2 spectra, where the presence of titanium, oxygen and carbon can be observed, however silver is present as well. Silver particles were spotted in different points. Carbon grids were used for SEM analysis, hence the presence of carbon in the spectra. Overall the EDS analysis provided a semi-quantitative elemental analysis of the surface showing that Ti and Ag appeared on the surface.

1.1.1.4 Fourier Transform Infra-red Spectroscopy (FTIR)

Fourier transform infra-red spectroscopy **(**FTIR**)** was used to identify the functional groups in the prepared pristine TiO_2 and Ag-TiO_2 thin films**.**

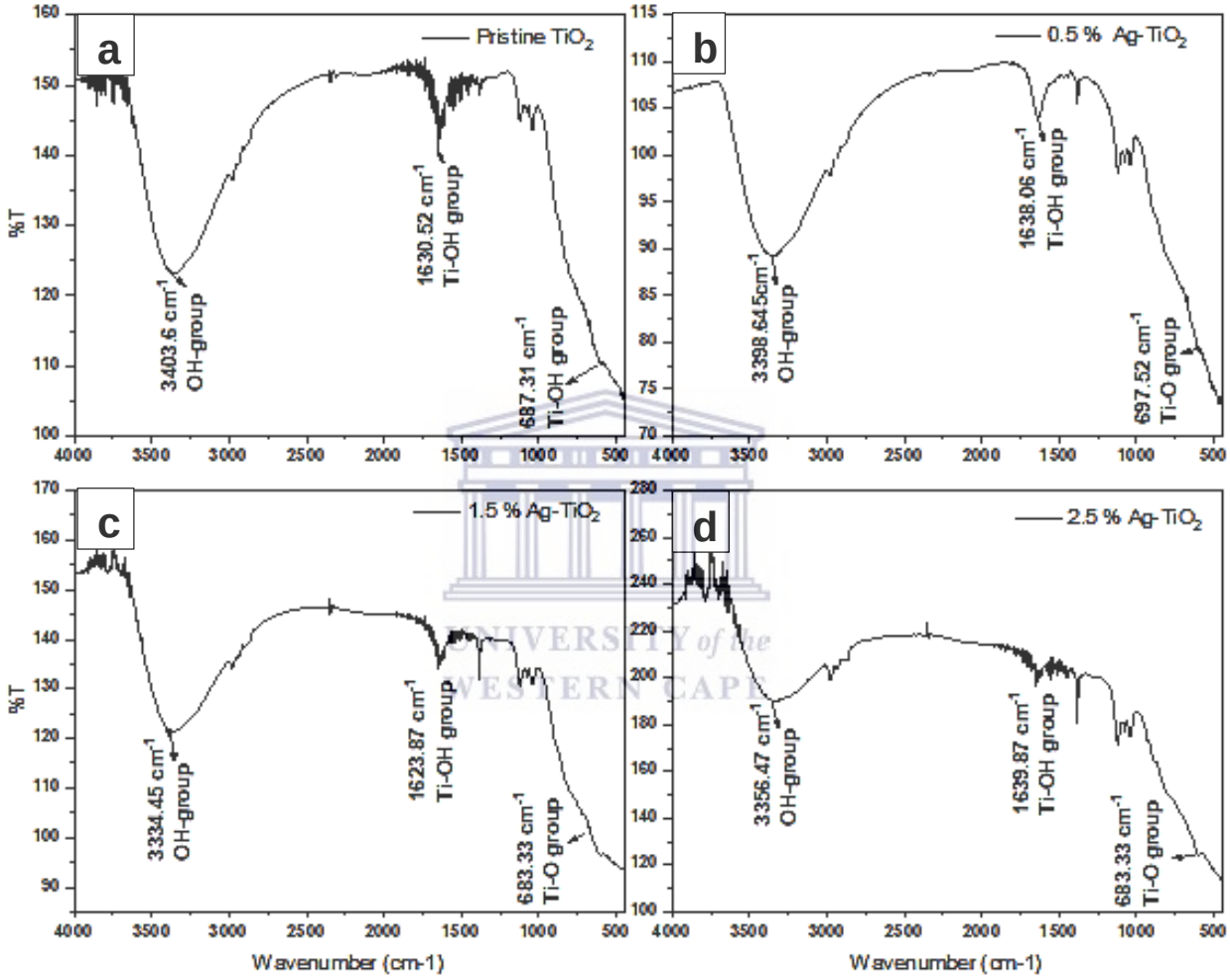

Figure 4.7: FTIR spectra of a) pristine TiO_2, b) 0.5% Ag-doped TiO_2, c) 1.5% Ag-doped TiO_2 and d) 2.5 % Ag-doped TiO_2 thin films on ITO substrates recorded at room temperature.

Figure 4.7 a), b), c) and d) shows the FTIR spectra of the pristine TiO_2 and Ag-TiO_2 thin films prepared at different percentage doping. From the vibration bands obtained from the spectra of each of the analyzed films, we can notice the presence of a broad band appearing in the range of

3330-3400 cm^{-1} which is attributed to the O-H stretching vibration and band in the range of 1630-1640 cm^{-1} attributed to Ti-O-H bending vibration which is present as a result of the chemically adsorbed water molecules. The broad band at 450-850 cm^{-1} represents the Ti-O bending mode of vibrations which corroborates the presence of metal oxygen bonding [2].

4.1.5 Optical Absorption

1.1.1.5 UV-Visible Spectroscopy (UV-Vis)

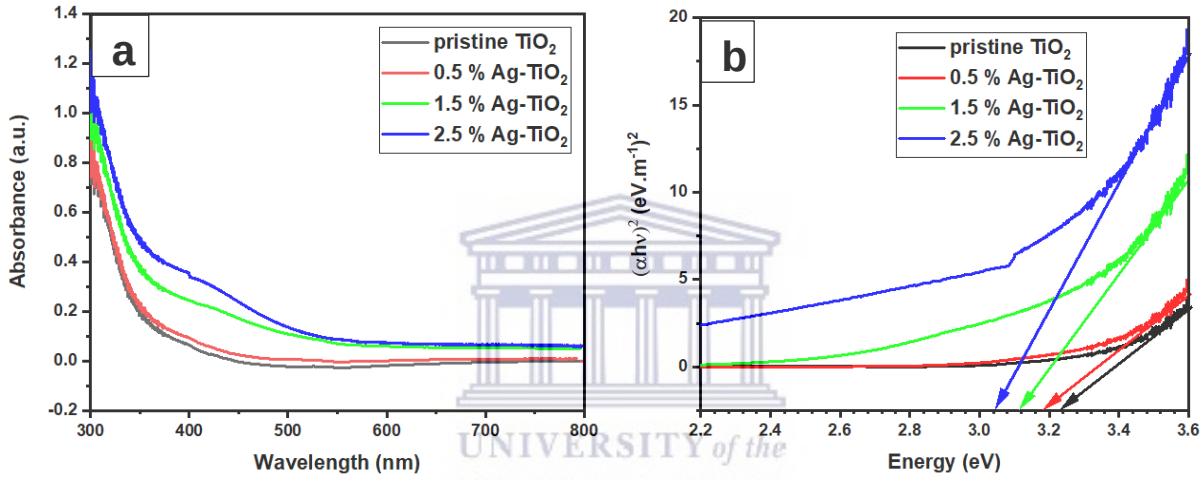

Figure 4.8: a) UV-Vis absorption spectra of pristine TiO_2 and Ag-TiO_2 composite compact films b) Tauc plot for bandgap calculation of the pristine TiO_2 and Ag-TiO_2 composite compact films.

The UV–Vis absorption spectra results are shown in **Figure 4.8 a)**. By doing a comparison of the optical absorption curves of the Ag-TiO_2 composite compact film, it is clear that, as the percentage of Ag augments, the absorption is progressively enhanced; the 2.5% Ag/nano-TiO_2 composite compact film shows the highest amount of absorption. The Ag-TiO_2 composite samples have higher absorption than the samples that do not contain Ag in the visible light region, which is mostly attributed to the surface plasmon resonance (SPR) of the metallic Ag nanoparticles in the Ag-TiO_2 composite compact film [3–6].

Figure 4.8 b) shows the Tauc plot obtained from the absorption of the undoped and Ag doped TiO_2 films. The graph was rescaled on the x-axis so it starts from 2.2 eV and ends at 3.6 to make

sure the area of interest was highlighted and clearly visible. As the ratio of Ag doping rises from 0% mol to 2.5 % mol, the band gap values are reduced. It can be observed that the band gap and absorbance spectra corroborate each other. These observed findings demonstrate that doping can potentially decrease the width of the forbidden band of TiO_2 thin films. The range of values found in the literature for the band gaps of anatase lie between 3.20 and about 3.56 eV [7]. In our specific study, though the band gap of undoped TiO_2 film is 3.23 eV, it obviously decreased to 3.04 for 2.5 % mol Ag doped TiO_2 film. A potential process behind the decreasing band gap of Ag-doped TiO_2 films could be that lattice distortion occurred with doping Ag ions in TiO_2 and produced the contamination level in the forbidden band of TiO_2. Adsitionaly, it can be speculated that fermi level of TiO_2 is higher than that of loaded silver. Silver deposits behave as buildup/accumulation sites for photo-generated electrons transferred from TiO_2 [8]. Effective separation of electrons and holes can therefore be reached by raising the silver content up to the optimum proportion.

The trend observed with the reduction in band gap as the Ag percentage doping is increased is indicative that the impact of silver within a perovskite solar cell device would be that of increasing the the light absorption of the electron transport layer (ETL) therefore allowing the absorbing layer to use the light received much more efficiently, which in turn could ultimately result in an improvement of the overall power conversion efficiency of the device.

Table 4.1: Band gap values of the undoped TiO_2 and Ag doped TiO_2.

Film	Eg (eV)
0 % Ag-TiO_2	3.23
0.5 % Ag-TiO_2	3.18
1.5 % Ag-TiO_2	3.11
2.5 % Ag-TiO_2	3.04

4.1.6 Electrochemistry

1.1.1.6 Cyclic Voltammetry (CV)

In order to evaluate the electronic behavior of the blocking layer, cyclic voltammetry study was done. The electro-activity of the prepared thin films was investigated using a 5 mM $K_3Fe(CN)_6$ in 0.1 M KNO_3 electrolyte. The potential window used for the investigation was -1.0 V to +1.0 V. The precursor materials that were investigated were bare ITO, pristine TiO_2 coated ITO, 0.5 % Ag-TiO_2 coated ITO, 1.5 % Ag-TiO_2 coated ITO and 2.5 % Ag-TiO_2 coated ITO. It is important to note that the bare ITO was also studied to clearly observe the trends in changes in conductivity of the coated layers by comparison. Scan rates of 10 mV/s, 50 mV/s and 100 mV/s were studied for each of the layers studied, but 50 mV/s was chosen as the optimal scan rate which was used ultimately used for the study.

A three-electrode system comprising of working electrode, counter electrode and reference electrode was used. The working electrode used was ITO coated glass substrate coated with the materials while the counter electrode was a platinum electrode and the reference electrode used was a Ag/AgCl reference electrode in 3 M KCl. As scan rate was initiated, potential was applied to the material within the potential window, at a characteristic potential value the materials responded with a current peak assuming they exhibit electrochemical behavior within that window. The voltammograms of the precursor materials that showed cathodic and anodic peaks are summarized in **Figure 4.8 a)** to **d)**.

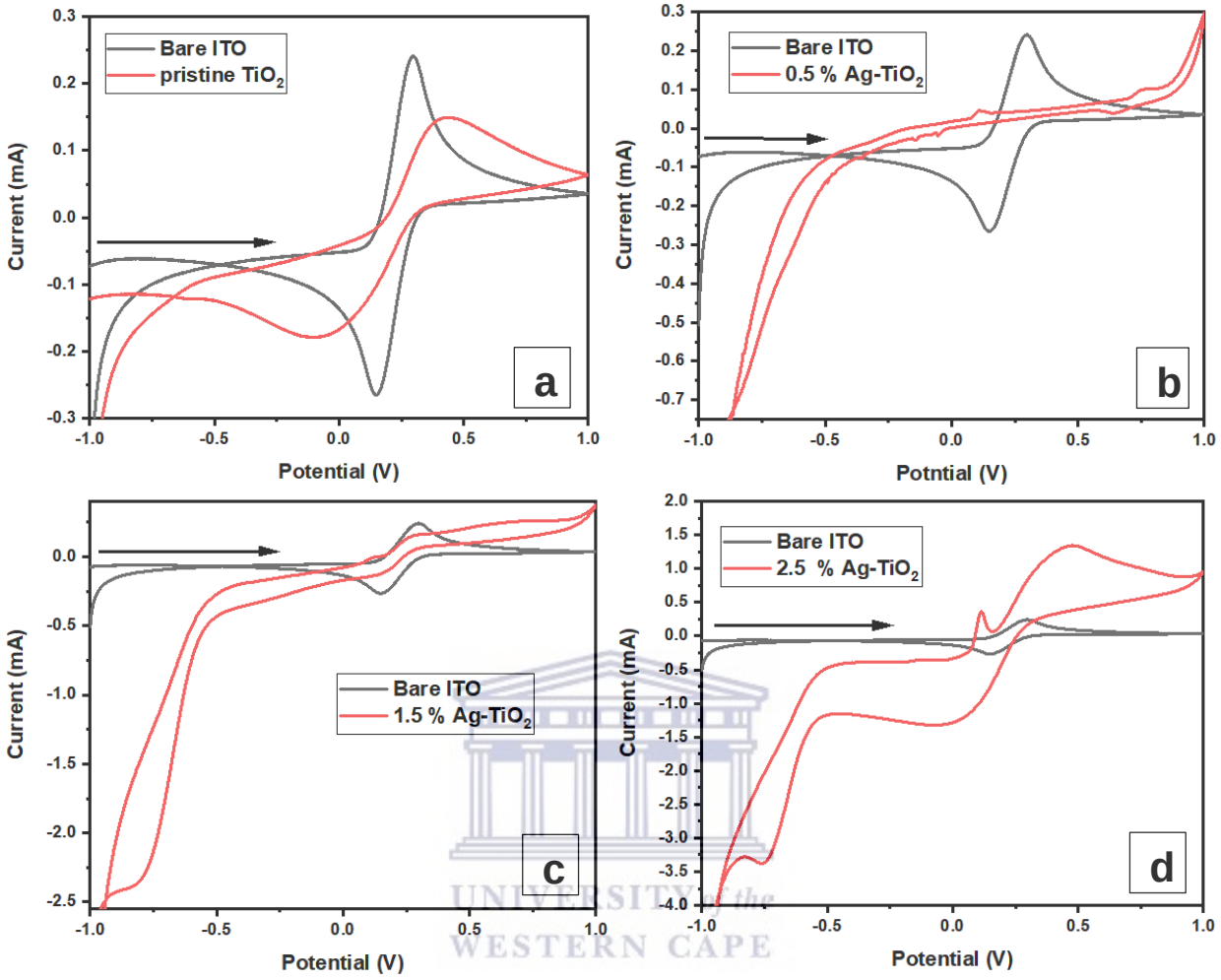

Figure 4. 9: Cyclic voltammograms of a) bare and TiO_2 coated ITO b) bare and 0.5 Ag-TiO_2 coated ITO c) bare and 1.5 % Ag-TiO_2 coated ITO and d) bare and 2.5 % Ag-TiO_2-coated ITO. The analyses are recorded at scan rate of 50 mV. s^{-1} in a 5 mM of $K_3Fe(CN)_6$ with 0.1 M KNO_3.

As seen in **Figure 4. 9 a),** the presence of the spin-coated pristine TiO_2 slightly decreases the anodic and cathodic currents with respect to a bare ITO electrode which is in this case very good as it confirms the assumption we made in the morphological analysis that there were no observable pinholes on the surface of the layer. However the shape of the curves, the peaks shift and the current variations, do suggest some substantial change of the electrode surface as already confirmed by the morphological analysis.

Compared to **Figure 4.** 9 **a)**, the behavior of the 0.5% Ag-TiO_2 is much different as seen in the cyclic voltammogram shown in **Figure 4.** 9 **b)**. Here, what is observed is that there is a much larger decrease the anodic and cathodic currents with respect to the bare ITO electrode not at very negative potentials. This decrease is accompanied by the appearance of much smaller cathodic and anodic peak which are quasi inexistent at -0.1 and 0.4 V, which in this case would be associated to the influence of the Ag nanoparticles. However the trend observed with the increase in Ag percentage observed in **Figure 4. 9 b)** through to **d)** is that there is once again an increase in anodic and cathodic peak currents. This is an indication that even though the TiO_2 is acting as a blocking layer limiting the interaction between the electrolyte and the ITO electrode, the presence of the Ag within the TiO_2 layer makes the substrate more conductive. This trend alone is indicative that the impact of silver within a perovskite solar cell device would be that of increasing the electron charge transfer to the electron transport layer (ETL) and which could ultimately result in an improvement of the overall power conversion efficiency of the device.

4.2 Device characterization

4.2.1 I-V measurements

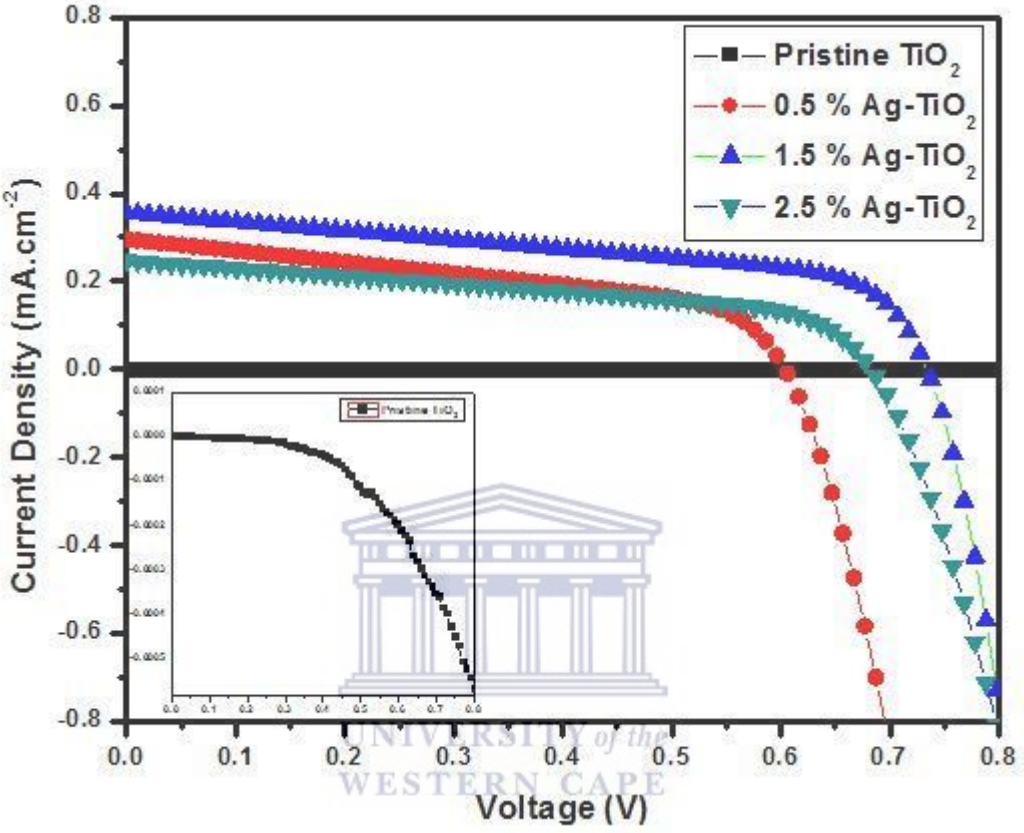

Figure 4.10: I-V characteristics of PSC devices based on different contents of Ag-TiO_2 composites compact films under AM 1.5G irradiation (100 $mW.cm^{-2}$).

The PSC devices' performance was evaluated under AM 1.5G irradiation (100 mW cm^{-2}). Each Each step involved in the fabrication the PSC device was done in ambient air and at a moisture level of about 60%. Humidity was one big issue that had to be addressed as the device degradation was accelerated by it. Then, the PSC devices were kept in a drying box. The I–V curves of the PSCs with the pristine compact film and the 0.5, 1.5, and 2.5 % Ag-TiO_2 composite compact films are shown in **Figure 4.10** and the corresponding photovoltaic parameters are listed in **Table 4.2**.

The data in **Table 4.2** demonstrate that J_{SC} improves progressively with the increase Ag amount except for the 2.5% Ag-TiO_2; the PSC device with the 1.5% Ag-TiO_2 composite compact film has the highest Jsc and achieves 0.36 mA.cm^{-2}. However, with the increase in the content of Ag, the PSC device with the 2.5% Ag/nano-TiO_2 composite compact film has the lowest J_{SC} and PCE, because a high content of Ag lowers the electron conducting role of the TiO_2 and the Ag impurities also act as a recombination center, resulting in lower J_{SC} and PCE values [9].

Table 4.2: Summarized parameters of PSC devices based on 0-2.5 % Ag-TiO2 composite compact film.

Samples	V_{oc} (V)	J_{sc} (mA.cm^{-2})	FF (%)	PCE (%)
0 % Ag-TiO_2	0.17	0.15	0.36	0.01
0.5 % Ag-TiO_2	0.60	0.30	0.50	0.09
1.5 % Ag-TiO_2	0.73	0.36	0.51	0.14
2.5 % Ag-TiO_2	0.70	0.25	0.48	0.08

It can also be observed from **Table 4.2** that the open-circuit voltage (V_{OC}) difference is quite important for the PSC devices with different contents of the Ag-TiO_2 composite compact film. It is known that V_{OC} is determined by the CB of TiO_2 and the perovskite in the PSC device, which means that the addition of Ag into the TiO_2 nanocrystal has had a significant impact on the CB of TiO_2. In general, the perovskite solar cell with the 1.5% Ag–TiO_2 composite compact film exhibits the highest PCE of 0.14 % and J_{SC} of 0.36 mA cm^{-2}, representing a 140 and 130 % increase compared to the PSC device without Ag. The percentage increase is extremely high, so one reason for this could be whether the layers were compact enough and well deposited on top of each other during the fabrication process as any irregularities during that process could potentially affect these parameters which may results in situation such as this.

4.3 References

[1] W. Li, R. Liang, A. Hu, Z. Huang, Y.N. Zhou, Generation of oxygen vacancies in visible light activated one-dimensional iodine TiO2 photocatalysts, RSC Adv. 4 (2014) 36959–36966. doi:10.1039/c4ra04768k.

[2] O.F. Tio, S. Composites, A.N. Murashkevich, A.S. Lavitskaya, T.I. Barannikova, I.M. Zharskii, Infrared Absorption Sectra and structure of TiO_2-SiO_2 composites, J. Appl. Spectrosc. 75 (2008) 724–728.

[3] J. He, I. Ichinose, S. Fujikawa, T. Kunitake, A. Nakao, Reversible conversion of nanoparticles of metallic silver and silver oxide in ultrathin TiO_2 films: A chemical transformation in nano-space, Chem. Commun. 8 (2002) 1910–1911. doi:10.1039/b204227b.

[4] D.W. Brandl, P. Nordlander, Plasmon modes of curvilinear metallic core/shell particles, J. Chem. Phys. 126 (2007). doi:10.1063/1.2717167.

[5] K. Kawahara, K. Suzuki, Y. Ohko, T. Tatsuma, Electron transport in silver-semiconductor nanocomposite films exhibiting multicolor photochromism, Phys. Chem. Chem. Phys. 7 (2005) 3851–3855. doi:10.1039/b511489f.

[6] K. Matsubara, T. Tatsuma, Morphological changes and multicolor photochromism of Ag nanoparticles deposited on single-crystalline TiO2 surfaces, Adv. Mater. 19 (2007) 2802–2806. doi:10.1002/adma.200602823.

[7] A. Nakaruk, D. Ragazzon, C.C. Sorrell, Anatase-rutile transformation through high-temperature annealing of titania films produced by ultrasonic spray pyrolysis, Thin Solid Films. 518 (2010) 3735–3742. doi:10.1016/j.tsf.2009.10.109.

[8] Y. Cao, H. Tan, T. Shi, T. Shi, T. Tang, J. Li, Preparation of Ag-doped TiO_2 nanoparticles for photocatalytic degradation of acetamiprid in water, J. Chem. Technol. Biotechnol. 83 (2008) 546–552. doi:10.1002/jctb.1831.

[9] B. Xin, L. Jing, Z. Ren, B. Wang, H. Fu, Effects of Simultaneously Doped and Deposited Ag on the Photocatalytic Activity and, J. Phys. Chem. B. 109 (2005) 2805–2809.

Chapter 5 Conclusions and Future work

This chapter gives a summary of the outcome of the research done in this thesis. It also gives recommendations with regards to some of the objectives that were not met and the way forward in order to improve and the results obtained from the J-V measurements of the solar cells.

5.1 Conclusions

Perovskite solar cells have had a substantial progression in terms of power conversion efficiency going from 3.8% to over 22% since 2012. Tandem perovskite-based solar cells have had an even better increase with PCEs reaching as high as 26.7%, setting a new record in the history of photovoltaic technology. A lot of research efforts have been put in place in order to both improve PSCs efficiency and attain a much deeper understanding of the perovskite materials' outstanding electrical and optical properties, such as largely-tunable band gaps for light absorption, high absorption coefficients, large carrier diffusion lengths, great carrier mobility, have been established during the past few years. The PSCs currently researched on already have combined structural advantages of both DSSCs and thin film PV ever since the discovery of perovskite and have become one of the main contenders to Si-based PV dominant market share, not only owing to its record 22.1% efficiency for small area but also for comparable larger-area device efficiency.

With the above mentioned facts in mind, the aim of this project was to develop efficient and cost-effective solar cells through the process of synthesis, fabrication, optical and electrochemical characterization of Ag-TiO_2/Perovskite/ Spiro-OMeTAD-based PSCs. The PSCs were fabricated with different doping percentages of Ag in the electron transport layer which in this case was TiO_2 to form Ag-TiO_2 composite films. The addition of the Ag to the TiO_2 drastically improved the light absorption of the TiO_2 in the visible light region as was confirmed by the UV-Vis results and band gap values obtained from it. This same trend was also seen in the built PSCs devices. This improvement was due to the resonance plasmon effect of the metallic Ag nanoparticles present in the Ag-TiO_2 composite compact films. Due to the addition of the Ag nanoparticles, an improvement in the conductivity was observed as seen with CV

results which in turn decreased the charge transfer resistance of the PSC device and the cells performances clearly improved. However compared to the TiO_2 without Ag, only one device containing 1.5 % Ag-TiO_2 achieved higher PCE of 0.14%.

5.2 Recommendations

The above research project indicated that there is truly a great potential for PSCs if the stability the cells as well as fabrication process and conditions is improved. In this work as was observed in the results obtained from the J-V measurements very low current output was obtained leading to the overall efficiencies of the devices being very low. Therefore, in order to remediate to this issue, very careful attention needs to be put first of all on the layer deposition techniques used. We know form literature that the devices with the good and even layer homogeneity obtain in most cases the best efficiencies. Secondly careful attention needs to be put on the monitoring of the layer thickness as it is also a very critical parameter that needs to be taken into account if higher efficiencies are going to be achieved.